


## PAPER

[View Article Online](#)  
[View Journal](#) | [View Issue](#)Cite this: *Dalton Trans.*, 2025, **54**,  
12201**Ethylenediaminetetraacetic acid-modified  
halloysite nanotubes loaded with layered SnS<sub>2</sub> for  
highly efficient removal of methylene blue†**Lan Yang, Qiyan Lu, Xiao Zhou, Tao Yang and Chunfang Du \*

Adsorption is an effective strategy for treating water pollution and natural clay mineral-based materials exhibit great potential for removing pollutants from wastewater. In this paper, halloysite nanotubes (HNTs) modified with ethylenediaminetetraacetic acid (EDTA) were thermally treated to serve as supports for loading SnS<sub>2</sub> to construct SnS<sub>2</sub>/HNTs(C) (SHC<sub>x</sub>-y). Methylene blue (MB) was selected as a target pollutant to examine the removal efficiency of the obtained adsorbents. SHC<sub>0.04</sub>-500 could remove more than 90% of MB (50 mg L<sup>-1</sup>) within 18 min, which was 9 and 18 times higher than those of SnS<sub>2</sub> and HNTs(C)-500, respectively. Moreover, the adsorbent SHC<sub>0.04</sub>-500 with good pH and temperature adaptability exhibited excellent adsorption performance toward cationic dyes and various antibiotics. The adsorption process of MB over SHC<sub>0.04</sub>-500 matched well with the Langmuir isotherm and the pseudo-first-order kinetic model. The adsorption mechanism investigation suggested that the carbon layer on HNTs made the surface of SHC<sub>0.04</sub>-500 more negative, which mostly contributed to the improved adsorption performance. This work provides a low-cost, environmentally friendly, and efficient adsorbent for removing pollutants from wastewater and contributes a new strategy to enhance the removal efficiency by a simple modification method.

Received 14th June 2025,  
Accepted 12th July 2025

DOI: 10.1039/d5dt01400j

[rsc.li/dalton](http://rsc.li/dalton)**Introduction**

With the rapid development of modern industry, a large number of pollutants from textile, paint, leather, and other industries are discharged into water systems, which bring serious effects to the ecological environment and human health.<sup>1–6</sup> Therefore, it is urgent to find more efficient, economical, and environmentally friendly methods to remove pollutants from water.

At present, there are multiple available techniques for treating water pollutants, including photocatalytic degradation, Fenton reaction, adsorption and so on. The degradation process refers to the breaking of a large organic dye structure into small molecules, which may produce toxic or harmful chemicals if the degradation is insufficient.<sup>7–10</sup> Compared to degradation, adsorption has received much attention because of its simplicity, low cost, safety, and non-toxicity.<sup>11</sup> A large number of adsorbents such as biochar, graphene oxide, and MOF composites have been applied in the removal of organic

pollutants.<sup>12–14</sup> However, the specific surface area and porosity of the above adsorbents are generally affected by the raw materials and preparation conditions, leading to an uncontrollable adsorption efficiency.<sup>15</sup> Natural clay minerals have the advantages of large specific surface area, stable structure, and easy modification. It has been reported that the combination of minerals and adsorbents can overcome the shortcomings mentioned above and be a potential strategy for water pollution treatment.<sup>16,17</sup> Halloysite nanotubes (HNTs) are composed of curled silicate layers with a hollow tubular morphology.<sup>18</sup> The inner and outer walls of HNTs are composed of alumina octahedra and silica-oxygen tetrahedra, respectively, both of which contain a certain number of hydroxyl groups.<sup>19</sup> This structural characteristic indicates that the chemical modification of HNTs could be easily achieved. Moreover, HNTs have a rich porous structure, a large specific surface area, a high aspect ratio, and low cost.<sup>20,21</sup> In recent years, the application of HNTs in water treatment has been further explored. For instance, HNTs modified with (3-aminopropyl) triethoxysilane (H-APTES) exhibited excellent removal efficiencies toward both Cu<sup>2+</sup> ions and reactive red 120 azo dye (RR-120).<sup>22</sup> A MgAl-LDH/HNT composite showed a highly efficient CO<sub>2</sub> adsorption performance with an adsorption capacity of 3.91 mmol g<sup>-1</sup>.<sup>23</sup> Thus, HNTs could be a potential and ideal material to construct functional mineral composites for removing water pollutants.<sup>24,25</sup>

College of Chemistry and Chemical Engineering, Inner Mongolia University, Hohhot, Inner Mongolia, 010021, P. R. China. E-mail: [cedchf@imu.edu.cn](mailto:cedchf@imu.edu.cn);

Fax: +86-471-4994375; Tel: +86-471-4994375

† Electronic supplementary information (ESI) available. See DOI: <https://doi.org/10.1039/d5dt01400j>

Recently,  $\text{SnS}_2$  has received increasing attention in water treatment due to its good adsorption performance, stable chemical properties, and simple synthesis.<sup>26–28</sup>  $\text{SnS}_2$  nanoparticles exhibited an adsorption efficiency of 85% toward rhodamine B within 180 min.<sup>29</sup> Compared to  $\text{SnS}_2$  with other morphologies, layered  $\text{SnS}_2$  could remove a large number of toxic organic dyes by selective adsorption, which further highlighted its advantages in pollutant removal.<sup>30</sup> Moreover, the layered structure could effectively improve the diffusion of dye molecules, provide better transport paths, and offer a large number of adsorption sites for the adsorption process.

It was reported that the carbon modification of HNTs could bring about an expansion of the specific surface area and an increase in the number of adsorption sites, which further improved the adsorption efficiency.<sup>31</sup> Thus, it is anticipated that composites constructed using HNTs with carbon modification and layered  $\text{SnS}_2$  could be ideal and potential adsorbents for removing water pollutants.<sup>32,33</sup>

In this work, HNTs modified with EDTA after calcination were used as supports for loading layered  $\text{SnS}_2$  to construct  $\text{SnS}_2/\text{HNTs}(\text{C})$  ( $\text{SHC}_{x-y}$ ) composites. The synthesized adsorbents possessed large specific surface areas, rich porous structure, and more negative surface charge, making them suitable for MB removal. The adsorption conditions including MB concentration, adsorbent dosage, temperature, and pH value were systematically optimized. The important role of carbon modification of HNTs in enhancing the removal efficiency was emphatically discussed. Moreover, the adsorption process of MB over  $\text{SHC}_{0.04-500}$  was examined and a plausible adsorption mechanism was put forward.

## Experimental

### Materials and methods

Halloysite nanotubes (HNTs) were purchased from Guangzhou Runwo Material Technology Co. Ltd. Ethylenediaminetetraacetic acid (EDTA) was purchased from Tianjin Xinbute Chemical Co. Tin chloride pentahydrate ( $\text{SnCl}_4 \cdot 5\text{H}_2\text{O}$ ) was purchased from Tianjin Beilian Fine Chemicals Development Co. Methylene blue (MB) was purchased from Beijing Inokai Technology Co. Thiourea ( $\text{CH}_4\text{N}_2\text{S}$ ), sodium hydroxide (NaOH), hydrochloric acid (HCl), and absolute ethanol (EtOH) were purchased from Tianjin Fengchuan Chemical Reagent Technology Co. Malachite green (MG), methyl violet (MV), orange yellow (OA), and methyl orange (MO) were purchased from Aladdin Ltd. Norfloxacin (NFO), ofloxacin (OFX), and tetracycline hydrochloride (TC) were purchased from Shanghai Meryer Chemical Reagent Co. All reagents were used without further purification. The crystal structures of the samples were examined by X-ray diffraction (XRD, Empyrean Panalytical, Netherlands). The size and morphology of the samples were determined by scanning electron microscopy (SEM, HITACHI S-4800, Japan). Transmission electron microscopy (TEM) was performed using a Talos F200S G2 instrument. X-ray photoelectron spectroscopy (XPS) was performed using a Thermo Fisher K-alpha instrument, recording the surface elemental compositions and their chemical states. The changes of

molecular structure were studied by Fourier transform infrared spectroscopy (FT-IR, VERTEX70). The zeta potentials at different pH values were obtained using a Malvern Zetasizer Nano ZS90 instrument. The specific surface areas of the samples were obtained using the Brunner–Emmett–Teller method (BET, Quantachrome, USA). Raman spectra were recorded using a Horiba Scientific LabRAM HR Evolution spectrometer with an excitation wavelength of 325 nm over the range of 1000–2000  $\text{cm}^{-1}$ .

### Pretreatment of HNTs

HNTs (2.5 g) were dispersed in deionized water (150 mL) under ultrasonic treatment for 30 min. EDTA (7.5 g) was dissolved in the above solution and kept at 80 °C for 24 h. Subsequently, the solid was centrifuged, washed with deionized water and ethanol several times, and dried at 60 °C overnight. The powders were calcined under an air atmosphere at different temperatures for 3 h (6 °C  $\text{min}^{-1}$ ) in a muffle furnace. The obtained products were named  $\text{HNTs}(\text{C})-y$  ( $y$  indicates the calcination temperature for HNTs,  $y = 400, 500, 600$ , and 800 °C).

### Synthesis of $\text{SHC}_{x-y}$

A series of  $\text{SnS}_2/\text{HNTs}(\text{C})$  samples were synthesized by a one-pot hydrothermal method. In a typical synthesis process, different amounts of  $\text{HNTs}(\text{C})-500$ , 0.14 g of  $\text{SnCl}_4 \cdot 5\text{H}_2\text{O}$ , and 3.12 g of thiourea were dispersed and dissolved in 35 mL of deionized water with stirring for 30 min. The mixture was kept at 180 °C for 18 h in a Teflon reactor. The samples were cooled to room temperature and washed with deionized water and ethanol alternately several times and dried at 60 °C overnight. The obtained products were named  $\text{SHC}_x-500$  ( $x$  indicates the different amounts of  $\text{HNTs}(\text{C})-500$ ,  $x = 0.04, 0.1, 0.3$ , and 0.5 g). For comparison, pure  $\text{SnS}_2$  was also prepared by using the same synthesis method as the composites just without the addition of  $\text{HNTs}(\text{C})-500$ .

### Adsorption experiment

In a typical adsorption experiment, 20 mg of  $\text{SHC}_{0.04-500}$  was dispersed in 20 mL of MB (50  $\text{mg L}^{-1}$ ) solution at room temperature. A certain amount of the suspension was removed and filtered at 3 min intervals. The concentration of MB was analyzed by UV-Vis spectroscopy. The adsorption efficiency (%) and adsorption capacity ( $q_e$ ) were calculated from eqn (1) and (2), respectively:

$$\text{Adsorption efficiency (100\%)} = \frac{(C_0 - C_t)}{C_0} \quad (1)$$

$$q_e = \frac{(C_0 - C_e)V}{M} \quad (2)$$

where  $C_0$  is the initial concentration of MB,  $q_e$  is the adsorption capacity,  $V$  is the volume of MB, and  $M$  is the mass of the adsorbent.  $C_t$  and  $C_e$  are the concentrations at moment  $t$  and at adsorption equilibrium, respectively.

In order to investigate the wide applicability of the adsorbent, various organic dyes (MV, OA, and MO) and antibiotics

(OFX, NFO, and TC) were selected to conduct adsorption tests. The concentrations of the above pollutant solutions were all  $50 \text{ mg L}^{-1}$ .

### Recycling experiment

The SHC<sub>0.04</sub>-500 sample after the adsorption experiment was dispersed in anhydrous methanol and stirred for 24 h. After centrifugation, it was dried overnight in an oven at  $60^\circ\text{C}$  and then reused in the subsequent adsorption experiments.

## Results and discussion

### Synthesis and structural characterization

In order to analyze the morphology and structure of pure and composite samples, SEM and TEM techniques were adopted. As shown in Fig. 1a, pure HNTs have a tube structure with a length of approximately  $1\text{--}2 \mu\text{m}$  and a diameter of  $50\text{--}100 \text{ nm}$ . The modified HNTs maintained the tubular morphology and smooth surface of pure HNTs, suggesting that calcination at  $500^\circ\text{C}$  had little effect on the tubular morphology of HNTs (Fig. 1b). As shown in Fig. 1c, SnS<sub>2</sub> was stacked by smooth hexagonal-like nanosheets with a diameter ranging from  $50$  to  $500 \text{ nm}$ . The SEM image of SHC<sub>0.04</sub>-500 (Fig. 1d) demonstrated that SnS<sub>2</sub> nanosheets come in close contact with HNTs(C)-500 nanotubes, enhancing the dispersion of SnS<sub>2</sub> in the composite and thereby more active sites could be exposed.

Fig. 2a shows the TEM image of SHC<sub>0.04</sub>-500. It could be clearly observed that SnS<sub>2</sub> nanosheets were uniformly anchored on the surface of HNTs(C)-500, demonstrating the successful synthesis of SHC<sub>0.04</sub>-500. The red area in the HRTEM image signifies the amorphous graphite carbon, indicating the anticipated carbon modification of HNTs (Fig. 2b). Additionally, the lattice spacing of  $0.27 \text{ nm}$  was indexed to the (101) crystal plane of SnS<sub>2</sub>, verifying the well-crystallized structure of SnS<sub>2</sub> in the composite. In Fig. 2c, carbon was found to be uniformly distributed across the entire structure, further confirming the successful carbon modification of HNTs. Notably, Al and Si elements were detected in the tubular

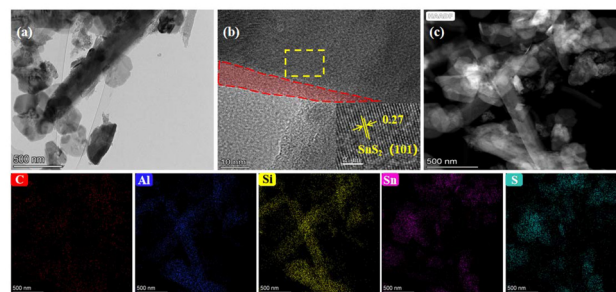


Fig. 2 TEM (a), HRTEM (b), and TEM elemental mapping images (c) of SHC<sub>0.04</sub>-500.

regions, while Sn and S elements were concentrated in the hexagonal lamellar domains. This spatially correlated elemental distribution provided direct evidence for the intimate integration of HNTs(C)-500 and SnS<sub>2</sub>, further confirming the successful synthesis of the SHC<sub>0.04</sub>-500 composite.

To further elucidate the detailed structural information and compositions of all samples, XRD and FT-IR techniques were adopted. The XRD patterns of HNTs and pure SnS<sub>2</sub> matched well with the standard PDF cards of HNTs and SnS<sub>2</sub> (JCPDS No. 09-0453 and JCPDS No. 23-0677), respectively (Fig. 3a). The characteristic peaks located at  $15.0^\circ$ ,  $32.1^\circ$ , and  $41.9^\circ$  correspond to the (001), (101), and (102) crystal planes of SnS<sub>2</sub>, respectively. The broad peak at  $24^\circ$  in the XRD pattern of HNTs(C)-500 indicates the presence of amorphous carbon.<sup>34,35</sup> The carbon layer might make it difficult to detect the characteristic peaks of HNTs.<sup>36</sup> Therefore, SHC<sub>0.04</sub>-500 obviously showed the diffraction peaks of SnS<sub>2</sub>, and the intensity of the SnS<sub>2</sub> diffraction peaks increased with a decrease in the addition amount of HNTs(C)-500 (Fig. S1†).

The FT-IR spectra of the pure and composite samples are shown in Fig. 3b. The absorption peaks at  $542$  and  $912 \text{ cm}^{-1}$  in HNTs belong to the bending vibration of Al–O–Si and the deformation vibration of Al–OH, respectively.<sup>37</sup> The absorption

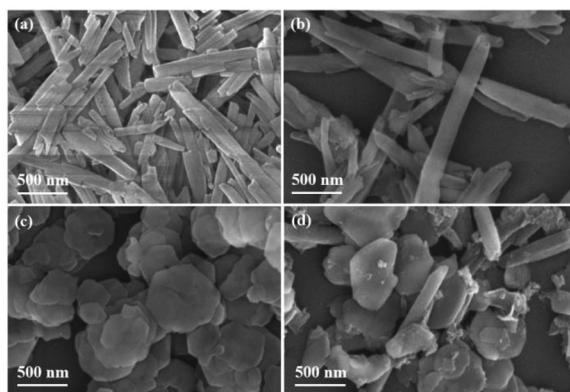


Fig. 1 SEM images of HNTs (a), HNTs(C)-500 (b), SnS<sub>2</sub> (c), and SHC<sub>0.04</sub>-500 (d).

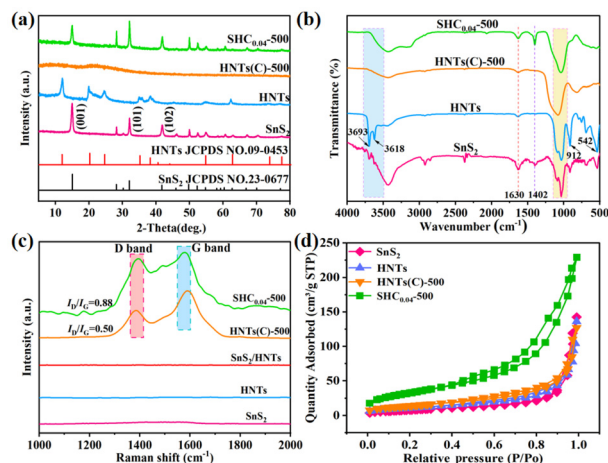


Fig. 3 XRD patterns (a), FT-IR spectra (b), Raman spectra (c), and N<sub>2</sub> adsorption-desorption isotherms (d) of various samples.

peaks at 1022 and 1107  $\text{cm}^{-1}$  correspond to the stretching vibrations of Si–O–Si and Si–O bonds in HNTs, respectively. In the spectrum of  $\text{SnS}_2$ , the characteristic peak at 1402  $\text{cm}^{-1}$  was attributed to the vibration of Sn–S bonds.<sup>38</sup> For  $\text{SnS}_2$  and HNTs, the absorption peaks at 3618 and 3693  $\text{cm}^{-1}$  were attributed to the stretching vibrations of the hydroxyl groups on the surfaces of  $\text{SnS}_2$  and HNTs, respectively.<sup>16</sup> Notably, the two broad peaks near 1100 and 3600  $\text{cm}^{-1}$  disappeared after HNT modification, indicating that the hydroxyl groups were removed from the surfaces of HNTs after high-temperature calcination.<sup>39</sup> All samples showed the peak at 1630  $\text{cm}^{-1}$ , which was attributed to the adsorbed water molecules. It was noteworthy that the peak at around 1000  $\text{cm}^{-1}$  in  $\text{SHC}_{0.04}\text{-500}$  shifted compared with that in pure HNTs(C)-500, which might be caused by the formation of new Si–O–Sn bonds.<sup>40</sup> The above phenomenon proved the successful combination of  $\text{SnS}_2$  with HNTs(C)-500.<sup>41</sup> The intensity of the peak at 1402  $\text{cm}^{-1}$  in  $\text{SHC}_{0.04}\text{-500}$  increased in contrast to that of  $\text{SnS}_2$ , which might be due to that there was a strong interaction between the C–C bond in HNTs(C)-500 with the Sn–S bond in  $\text{SnS}_2$ .<sup>40</sup>

Raman spectrometry was employed to confirm the graphitization of various samples (Fig. 3c). There were two significant bands at 1385 and 1590  $\text{cm}^{-1}$  in  $\text{SHC}_{0.04}\text{-500}$  and HNTs(C)-500, which imply the point defect degree (D band) and the graphitic structures (G band), respectively. The intensity ratio of the D band to the G band ( $I_D/I_G$ ) is generally used to describe the degree of graphitization of samples. The larger the ratio, the greater the degree of graphitization, *i.e.*, more defects were produced. According to the Raman results, the  $I_D/I_G$  value of  $\text{SHC}_{0.04}\text{-500}$  (0.88) was significantly higher than that of  $\text{SnS}_2/\text{HNTs}$  (0), suggesting that the modification of HNTs with EDTA and subsequent calcination positively affected the graphitization of  $\text{SHC}_{0.04}\text{-500}$ .<sup>42</sup> The D and G bands were not observed in pure  $\text{SnS}_2$  and HNTs.

Fig. 3d shows the  $\text{N}_2$  adsorption–desorption isotherms of various samples. All the prepared samples exhibited type IV isotherms.  $\text{SHC}_{0.04}\text{-500}$  had an obvious hysteresis loop, which was characteristic of a mesoporous structure. The  $\text{SHC}_{0.04}\text{-500}$  sample exhibited the largest specific surface area (118.49  $\text{m}^2 \text{g}^{-1}$ ), which was larger than those of  $\text{SnS}_2$  (30.90  $\text{m}^2 \text{g}^{-1}$ ), HNTs (40.09  $\text{m}^2 \text{g}^{-1}$ ), and HNTs(C)-500 (52.24  $\text{m}^2 \text{g}^{-1}$ ). The larger specific surface area of  $\text{SHC}_{0.04}\text{-500}$  endowed it with more adsorption sites, which was favorable for enhancing the adsorption efficiency of  $\text{SHC}_{0.04}\text{-500}$ .

Fig. 4 shows the survey XPS spectra of  $\text{SnS}_2$ , HNTs, HNTs(C)-500, and  $\text{SHC}_{0.04}\text{-500}$  as well as the high-resolution XPS spectra of each element. Fig. 4a shows that Sn, S, O, Si, Al, and C elements were all present in the  $\text{SHC}_{0.04}\text{-500}$  sample. The high-resolution C 1s spectra are shown in Fig. 4b. The characteristic peaks appearing at 288.9, 286.5, and 284.8 eV were attributed to the O–C=O, C–O, and C–C bonds, respectively. The peak area of  $\text{sp}^2$  hybridized carbon (284.8 eV) increased from 60.48% (HNTs) to 73.64% (HNTs(C)-500), indicating that modification of HNTs with EDTA was beneficial for increasing the graphitic carbon content, which was consistent with the results of Raman analysis.<sup>43</sup> The content of C–C in  $\text{SHC}_{0.04}\text{-500}$

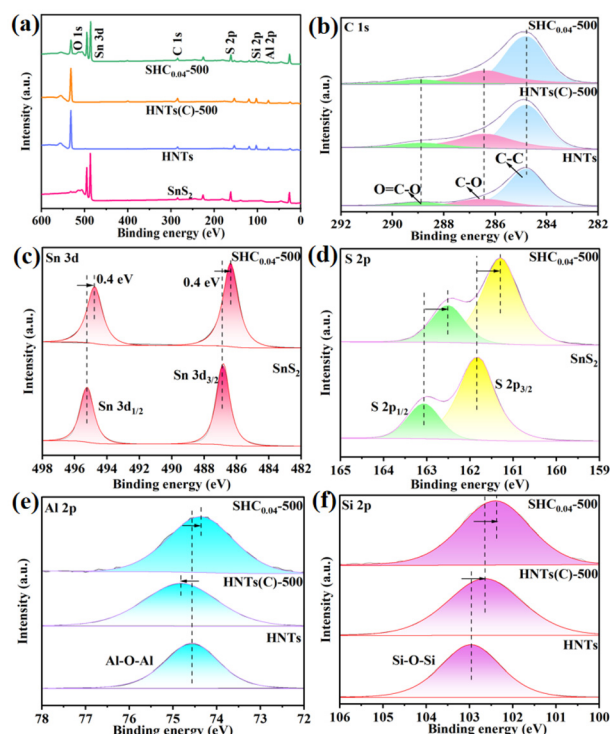


Fig. 4 Survey XPS spectra (a) and high-resolution spectra of C 1s (b), Sn 3d (c), S 2p (d), Al 2p (e), and Si 2p (f) of various samples.

was 70.6%, which was slightly smaller than that of C–C in HNTs(C)-500. This phenomenon suggested that some of C–C bonds in HNTs(C)-500 were broken and reorganized due to the interaction between  $\text{SnS}_2$  and HNTs(C)-500 during the synthesis process.<sup>44</sup>

As shown in Fig. 4c, Sn 3d spectra exhibited two binding energies at 494.8 and 486.4 eV, belonging to Sn 3d<sub>1/2</sub> and Sn 3d<sub>3/2</sub>, respectively. In comparison with pure  $\text{SnS}_2$ , the fitted peak of Sn 3d in  $\text{SHC}_{0.04}\text{-500}$  shifted to a lower-binding-energy position. In Fig. 4d, the characteristic peaks attributed to S 2p<sub>3/2</sub> and S 2p<sub>1/2</sub> orbitals shifted from 163.1 and 161.8 eV in  $\text{SnS}_2$  to 162.5 and 161.3 eV in  $\text{SHC}_{0.04}\text{-500}$ , respectively, which suggested that the presence of HNTs(C)-500 had an effect on the electronic state of  $\text{SnS}_2$ .<sup>45,46</sup>

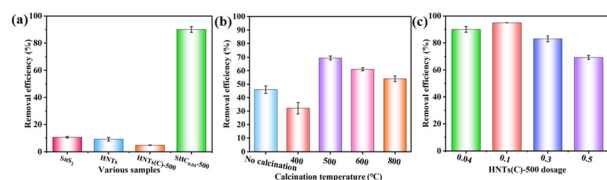
Fig. 4e and f separately show the characteristic peaks of Al 2p and Si 2p. For HNTs, both Al–O–Al and Si–O–Si bonds showed only one characteristic peak at 74.3 and 102.4 eV, respectively. In comparison with HNTs, the peak positions of Al 2p and Si 2p in  $\text{SHC}_{0.04}\text{-500}$  shifted to a lower binding-energy position. It was noteworthy that the binding energies of Sn 3d, S 2p, Al 2p, and Si 2p in  $\text{SHC}_{0.04}\text{-500}$  were all lower than those of pure  $\text{SnS}_2$  and HNTs(C)-500. This phenomenon not only confirmed the successful preparation of  $\text{SHC}_{0.04}\text{-500}$  but also provided direct evidence that  $\text{SnS}_2$  and HNTs(C)-500 were not merely physically mixed. Instead, their intrinsic electronic environments had been modified through interfacial interactions, which altered the electron distribution around these elements and thereby resulted in the observed decrease in binding energy.<sup>47</sup>

MB was selected as the target pollutant to investigate the removal performance of various samples. The  $\text{SnS}_2$ , HNTs, and HNTs(C)-500 samples could adsorb a small amount of MB with adsorption efficiencies of only 10.5%, 9.1%, and 5.0% within 18 min, respectively (Fig. 5a). The adsorption efficiency of  $\text{SHC}_{0.04}$ -500 was significantly improved, showing about 90% adsorption efficiency toward MB within 18 min, which was about 9, 10, and 18 times as those of  $\text{SnS}_2$ , HNTs, and HNTs(C)-500, respectively.

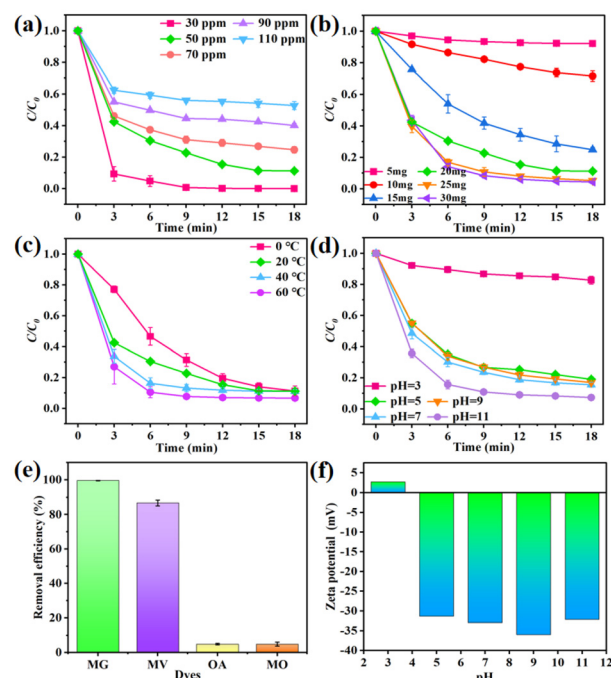
For exploring the optimal calcination temperature of modified HNTs, adsorption tests of MB over a series of  $\text{SHC}_{0.5-y}$  samples were performed. As shown in Fig. 5b, it could be observed that the adsorption efficiencies of the composites increased first and then decreased with increasing the calcination temperature of HNTs(C). At a lower temperature of 400 °C, the graphitization of the HNTs(C)-400 was low, which was not favorable for adsorption. When the calcination temperature reached 500 °C, the carbon in HNTs(C) formed a more regular graphite structure, resulting in a stronger interaction between the carbon layer and MB molecules, which could significantly improve the adsorption capacity.<sup>48</sup> However, with further increasing the temperature, the adsorption sites decreased due to the oxidation of the carbon layer on HNTs.<sup>49</sup> Based on the above analysis, 500 °C was adopted as the optimal calcination temperature in the following experiments.

Fig. 5c shows the effect of HNTs(C)-500 dosage on the adsorption efficiency of  $\text{SHC}_x$ -500. The adsorption efficiency increased first and then decreased with an increase of HNTs(C)-500 dosage. Based on the economic consideration, 0.04 g was selected as the optimal HNTs(C)-500 dosage in the subsequent experiments.

Fig. 6a shows the influence of MB concentration on the adsorption performance of  $\text{SHC}_{0.04}$ -500. The adsorption efficiency could reach more than 90% within 18 min, which decreased gradually with further increasing the initial MB concentration. The decreased adsorption efficiency indicated the insufficient active sites of  $\text{SHC}_{0.04}$ -500 for the enhanced number of MB molecules. Therefore, the initial MB concentration of 50  $\text{mg L}^{-1}$  was chosen for the next experiments. Fig. 6b shows the effect of  $\text{SHC}_{0.04}$ -500 dosage (5, 10, 15, 20, 25, and 30 mg) on the removal efficiency of MB. The adsorption efficiency increased obviously with an increase of  $\text{SHC}_{0.04}$ -500 dosage and reached 100% when the  $\text{SHC}_{0.04}$ -500 dosage was enhanced to 25 mg, which remain unchanged with further increasing the adsorbent dosage to 30 mg. This phenomenon might be explained by the increased number of active sites



**Fig. 5** The adsorption efficiencies of various samples (a), HNTs(C) at different calcination temperatures (b), and HNTs(C)-500 with different dosages toward MB (c).



**Fig. 6** Effects of MB concentration (a), adsorbent dosage (b), temperature (c), and pH value (d) on the adsorption efficiency of  $\text{SHC}_{0.04}$ -500. The adsorption efficiencies of  $\text{SHC}_{0.04}$ -500 toward various dyes (e). Effect of the pH value on the zeta potential of  $\text{SHC}_{0.04}$ -500 (f).

with increasing adsorbent dosage, leading to an increased adsorption efficiency.

In order to investigate the effect of temperature on the adsorption efficiency, adsorption experiments were carried out at different temperatures (0, 20, 40, and 60 °C) (Fig. 6c). It could be found that the temperature had no remarkable effect on the removal efficiency, just accelerated the adsorption rate of  $\text{SHC}_{0.04}$ -500 toward MB. From the point view of energy saving, 20 °C was selected as the optimal temperature for adsorption over  $\text{SHC}_{0.04}$ -500. Based on the above results, it could be deduced that the adsorbent  $\text{SHC}_{0.04}$ -500 had a promising application at variable temperatures.

The adaptability of an adsorbent in a wide pH range is very important for the practical application of the adsorbent. Fig. 6d shows the influence of pH value on the removal performance of  $\text{SHC}_{0.04}$ -500 toward MB. The adsorption efficiency reached 15% when the pH value was 3. As the pH value continued to rise, the adsorption efficiency showed a remarkable increase, which achieved the highest efficiency at pH = 11. This result demonstrated the adaptability of  $\text{SHC}_{0.04}$ -500 under conditions close to neutral and alkaline.

For investigating the applicability of  $\text{SHC}_{0.04}$ -500 to other dyes, adsorption experiments were carried out through selecting four different dyes as target pollutants (Fig. 6e). The cationic dyes MV and MG could be adsorbed over 85% to  $\text{SHC}_{0.04}$ -500. In contrast, the adsorbent showed very low adsorption efficiencies toward the anionic dyes OA and MO. Fig. 6f shows the zeta potential plots of  $\text{SHC}_{0.04}$ -500 at different pH values.

When the pH value was 3, the surface of the adsorbent was positively charged, resulting in a lower adsorption efficiency toward MB. In contrast, when the pH value was increased from 3 to 11, the surface was negatively charged, leading to a higher adsorption efficiency toward MB. It was obvious that the adsorbent showed the excellent adsorption performance toward cationic dyes, thus it could be deduced that the electrostatic attraction was possibly the key factor in the adsorption process.

The adsorption efficiencies of SHC<sub>0.04</sub>-500 toward various antibiotics with a concentration of 50 mg L<sup>-1</sup> were also examined (Fig. S2†). SHC<sub>0.04</sub>-500 showed the highest adsorption efficiency toward NFO, which was close to 80% within 18 min. The results indicated that SHC<sub>0.04</sub>-500 had great potential in removing antibiotics from wastewater.

The results of the cyclic adsorption experiments of MB over SHC<sub>0.04</sub>-500 are shown in Fig. 7a. The adsorption efficiency decreased by only 5% after the first cycle, which still remained 78% after the fourth cycle. The decreased adsorption efficiency was probably related to the incomplete desorption and adsorbent loss.<sup>50</sup> After the adsorption of MB, the color of the adsorbent changed from yellow to dark green, and the dark blue MB turned to light blue, suggesting that MB was successfully adsorbed by SHC<sub>0.04</sub>-500 (Fig. 7b).<sup>51</sup>

Fig. 7c demonstrates that the XRD pattern of SHC<sub>0.04</sub>-500 basically remains unchanged after the adsorption. A new peak at 1327 cm<sup>-1</sup> emerged in the FT-IR spectra of SHC<sub>0.04</sub>-500 after the adsorption, which was attributed to the C–C stretching vibrations of MB.<sup>52</sup> Moreover, two spurious peaks at 1244 and 1490 cm<sup>-1</sup> related to the C–N stretching vibration of N–CH<sub>3</sub> in the MB structure were also detected in SHC<sub>0.04</sub>-500 after adsorption, implying the successful adsorption of MB molecules on the surface of SHC<sub>0.04</sub>-500.<sup>53</sup> Based on the above analysis, it could be concluded that SHC<sub>0.04</sub>-500 exhibited excellent cycling and structural stability during the cycle tests.

Pseudo-first-order and pseudo-second-order models were employed to describe the adsorption process of SHC<sub>0.04</sub>-500

toward MB. The pseudo-first-order and pseudo-second-order equations are presented as formulas (3) and (4), respectively:<sup>54</sup>

$$\ln(q_e - q_t) = \ln q_e - k_1 t \quad (3)$$

$$\frac{t}{q_t} = \frac{1}{k_2 q_e^2} + \frac{1}{q_e} t \quad (4)$$

where  $q_t$  (mg g<sup>-1</sup>) and  $q_e$  (mg g<sup>-1</sup>) are the adsorption capacity of MB at time  $t$  and the equilibrium time, respectively.  $k_1$  and  $k_2$  are the related constants.

According to Fig. 8a, b, and Table S1,† the adsorption process of SHC<sub>0.04</sub>-500 toward MB had both physical and chemical adsorption. The adsorption data matched well with the pseudo-first-order model ( $R^2 = 0.99621$ ) than the pseudo-second-order model ( $R^2 = 0.99325$ ), implying that the physical adsorption played a dominant role in MB adsorption over SHC<sub>0.04</sub>-500.

From the above Raman results, it could be seen that SHC<sub>0.04</sub>-500 and HNTs(C)-500 had obvious G bands compared with HNTs, indicating that SHC<sub>0.04</sub>-500 and HNTs(C)-500 contained a large number of aromatic structures with  $\pi$  electron clouds. Due to the conjugated  $\pi$  bond structure of MB, it was attracted to SHC<sub>0.04</sub>-500 through  $\pi$ - $\pi$  stacking, causing their electron clouds to overlap and resulting in chemical adsorption. The results showed that carbonized HNTs played a certain role in promoting chemical adsorption.

The adsorption isotherm models are proposed to explain the adsorption equilibrium and express the interactions between adsorbent and adsorbed molecules.<sup>55</sup> In this study, four adsorption models were used to analyze the adsorption data, including Langmuir, Temkin, Redlich–Peterson, and Freundlich models. The specific model expressions are shown in eqn (5)–(8), respectively.

$$\frac{C_e}{q_e} = \frac{1}{q_m K_L} + \frac{C_e}{q_m} \quad (5)$$

$$q_e = A \ln(K_T C_e) \quad (6)$$

$$q_e = \frac{K_p C_e}{1 + \alpha C_e} \quad (7)$$

$$\ln q_e = \ln K_F + \frac{1}{n} \ln C_e \quad (8)$$

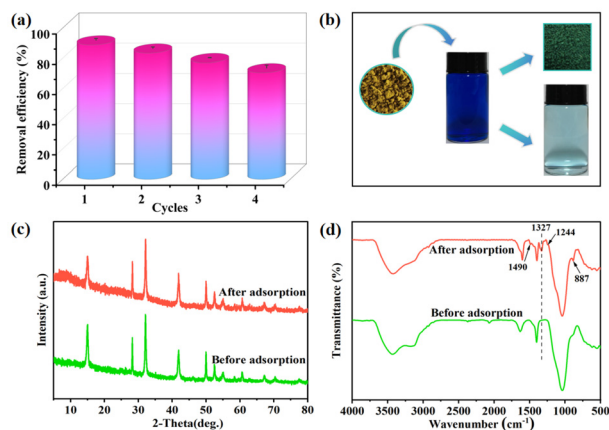


Fig. 7 The cycling performance of SHC<sub>0.04</sub>-500 (a). The color images of SHC<sub>0.04</sub>-500 and MB (b). XRD patterns (c) and FT-IR spectra (d) of SHC<sub>0.04</sub>-500 before and after adsorption.

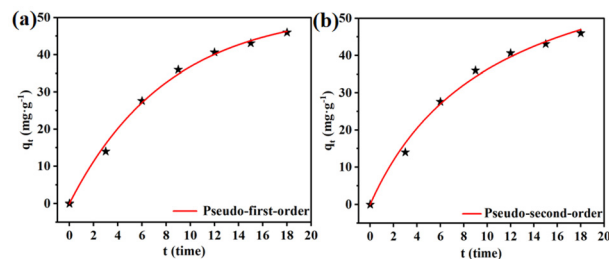


Fig. 8 The pseudo-first-order model (a) and the pseudo-second-order model (b) for MB adsorption over SHC<sub>0.04</sub>-500.

where  $C_e$  ( $\text{mg L}^{-1}$ ) and  $q_e$  ( $\text{mg g}^{-1}$ ) are the concentration of MB in solution and the adsorbed amount of the adsorbent at adsorption equilibrium, respectively, and  $q_m$  ( $\text{mg g}^{-1}$ ) is the maximum adsorbed amount of MB.  $K_L$ ,  $K_T$ ,  $K_P$ , and  $K_F$  are the Temkin, Langmuir, Redlich–Peterson, and Freundlich model adsorption constants, respectively.  $A$ ,  $\alpha$ , and  $n$  are the constants of the Temkin, Redlich–Peterson, and Freundlich models, respectively.

The fitting results of the four adsorption isotherm models are shown in Fig. 9 and Table S2.† The fitting coefficient of the Langmuir isotherm model ( $R^2 = 0.96934$ ) was higher than those of the Freundlich ( $R^2 = 0.91509$ ), Temkin ( $R^2 = 0.95782$ ), and Redlich–Peterson ( $R^2 = 0.96034$ ) isotherm models, suggesting that the Langmuir isotherm model could better describe the equilibrium data. The Langmuir model is based on the assumption of monolayer adsorption on the surface of a homogeneous adsorbent, where all adsorption sites are identical and there is no interaction between the adsorbed molecules.<sup>56</sup> Therefore, the adsorption of MB over SHC<sub>0.04</sub>-500 was monolayer adsorption.

As shown in Fig. S3,† HNTs(C)-500 exhibited a higher surface charge density than pristine HNTs, indicating that the carbon layer introduced the additional negative charges on the surface of HNTs(C)-500. In combination with the intrinsic charge properties of SnS<sub>2</sub>, the electrostatic attraction toward the cationic dye MB was undoubtedly enhanced. Notably, at pH > 3, all samples (HNTs, SnS<sub>2</sub>, HNTs(C)-500, and SHC<sub>0.04</sub>-500) have negative charges and SHC<sub>0.04</sub>-500 exhibited the highest value. This enhancement was possibly related to the covalent bond formation between SnS<sub>2</sub> and HNTs(C)-500 during the composite synthesis, which induced electron redistribution and thus increased the overall negativity of SHC<sub>0.04</sub>-500. Therefore, SHC<sub>0.04</sub>-500 exhibited significantly higher adsorption efficiency toward cationic dyes than anionic dyes, which was consistent with the principle of opposite charge

attraction. The kinetic and isotherm models revealed that the adsorption process conformed to the typical physical adsorption. The zeta potential data confirmed a strong relationship between the enhanced surface negativity of SHC<sub>0.04</sub>-500 and its superior MB adsorption performance. It can be concluded that the electrostatic attraction dominated the adsorption process of MB over SHC<sub>0.04</sub>-500.

Fig. S4 and Table S3† show the pore size distribution curves, surface areas, and pore size distribution data of various samples, respectively. HNTs(C)-500 had a larger specific surface area than HNTs, which suggested that the carbon layer on HNTs was beneficial for increasing the specific surface area. SHC<sub>0.04</sub>-500 had the largest specific surface area in comparison with those of HNTs, HNTs(C)-500, and SnS<sub>2</sub>. The larger specific surface area and smaller mesopores could provide more active sites, which was beneficial for enhancing the adsorption performance. The specific surface area and pore size of SHC<sub>0.04</sub>-500 changed after MB adsorption (Fig. S5 and Table S3†), although the changes were not significant. This indicates that only a small portion of MB molecules had attached to the surface and filled the pores of SHC<sub>0.04</sub>-500. Based on the above analysis, the large specific surface area and pore filling also contributed to the enhanced adsorption efficiency of SHC<sub>0.04</sub>-500 toward MB.

Moreover, the results of FT-IR spectroscopy suggested that a new peak at  $887\text{ cm}^{-1}$  emerged in the FT-IR spectrum of HNTs(C)-500. This new peak was attributed to the C–H bond, which could provide active sites for adsorption. The peak intensity of SHC<sub>0.04</sub>-500 at  $887\text{ cm}^{-1}$  increased after MB adsorption, indicating that the C–H bending vibration was affected. Thus, it could be deduced that there was a  $\pi$ – $\pi$  interaction between SHC<sub>0.04</sub>-500 and MB molecules, which was possibly another factor promoting the adsorption process.<sup>57</sup>

In summary, there were four main factors contributing to the enhanced adsorption performance of SHC<sub>0.04</sub>-500 toward MB, including electrostatic attraction, pore filling, large specific surface area, and  $\pi$ – $\pi$  interactions (Fig. 10).

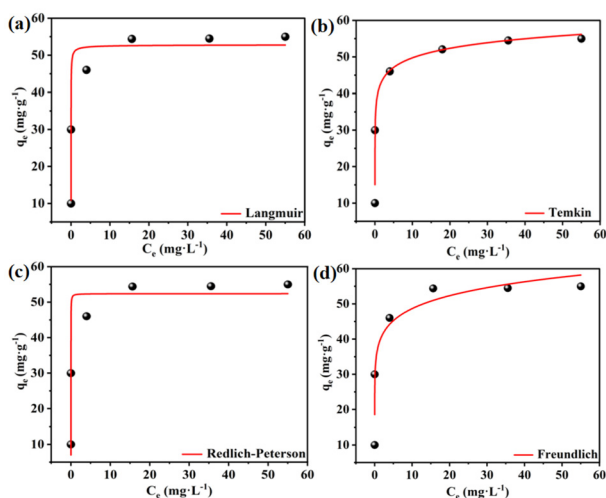


Fig. 9 Langmuir (a), Temkin (b), Redlich–Peterson (c), and Freundlich (d) isothermal models for MB adsorption over SHC<sub>0.04</sub>-500.

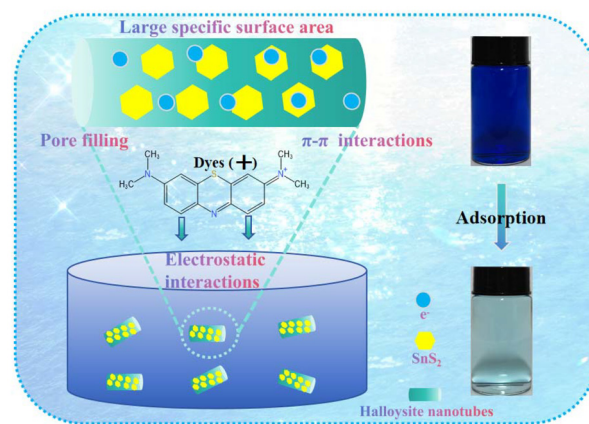


Fig. 10 The possible adsorption mechanisms of SHC<sub>0.04</sub>-500 toward MB.

## Conclusions

In this work, layered  $\text{SnS}_2$  was successfully anchored on the surface of EDTA-modified HNTs through a one-step hydrothermal method. The adsorbent  $\text{SHC}_{0.04}\text{-500}$  was able to remove 90% of MB ( $50 \text{ mg L}^{-1}$ ) within 18 minutes, showing higher adsorption efficiency compared to those of  $\text{SnS}_2$ , HNTs, and HNTs(C)-500. The synthesized adsorbent could be applied in the treatment of various cationic dyes and antibiotics, and displayed wide adaptability in a temperature range of 0–60 °C and a pH range of 3–11. Kinetics fitting results indicated that MB adsorption over  $\text{SHC}_{0.04}\text{-500}$  followed the pseudo-first-order model, and the Langmuir model was found to be a better fit for describing the adsorption process. The mechanism investigation results suggested that electrostatic attraction, pore filling, large specific surface area, and  $\pi$ – $\pi$  interactions contributed to the enhanced adsorption efficiency of  $\text{SHC}_{0.04}\text{-500}$ .

## Author contributions

Lan Yang designed and conducted the experimental studies, wrote the original manuscript, and conducted characterization studies. Qiyuan Lu gave some suggestions. Xiao Zhou made deep discussion. Tao Yang revised the manuscript. Chunfang Du supervised and commented on the manuscript.

## Conflicts of interest

There are no conflicts to declare.

## Data availability

The data that support the findings of this study are available from the corresponding author upon reasonable request.

## Acknowledgements

This work was supported by the National Natural Science Foundation of China (52164024 and 52374258) and the Post-Subsidy Funds for the Inner Mongolia Key Laboratory of Chemistry and Physics of Rare Earth Materials (2021PT0003).

## References

- 1 S. M. Zhai, M. Li, D. Wang, L. Zhang, Y. Yang and S. Fu, *J. Cleaner Prod.*, 2019, **220**, 460–474.
- 2 H. Zhang, G. Xue, H. Chen and X. Li, *Chemosphere*, 2018, **191**, 64–71.
- 3 Y. Qi, M. Yang, W. Xu, S. He and Y. Men, *J. Colloid Interface Sci.*, 2017, **486**, 84–96.
- 4 M. Arshadi, F. Mousavinia, M. J. Amiri and A. R. Faraji, *J. Colloid Interface Sci.*, 2016, **483**, 118–131.
- 5 M. M. Mian, G. Liu and H. Zhou, *Sci. Total Environ.*, 2020, **744**, 140862.
- 6 X. He, Y. Yang, Y. Li, J. Chen, S. Yang, R. Liu and Z. Xu, *Appl. Surf. Sci.*, 2022, **599**, 153898.
- 7 M. M. Vieira, A. S. P. Dornelas, T. D. Carlos, A. Pallini, C. Gravato, D. H. Pereira, R. A. Sarmento and G. S. Cavallini, *Chemosphere*, 2021, **283**, 131117.
- 8 H. Khadivi, M. Sirousazar, V. Abbasi-Chianeh and E. Jalilnejad, *J. Polym. Environ.*, 2022, **30**, 3186–3202.
- 9 C. Lei, M. Pi, C. Jiang, B. Cheng and J. Yu, *J. Colloid Interface Sci.*, 2017, **490**, 242–251.
- 10 Y. Li, B. Xing, X. Wang, K. Wang, L. Zhu and S. Wang, *Energy Fuels*, 2019, **33**, 12459–12468.
- 11 R. Zein, J. S. Purnomo, P. Ramadhani, Safni, M. F. Alif and C. N. Putri, *Arabian J. Chem.*, 2023, **16**, 104480.
- 12 B. Nissanka, N. Kottegoda and D. R. Jayasundara, *J. Mater. Sci.*, 2019, **55**, 1996–2005.
- 13 M. J. Uddin, R. E. Ampiauw and W. Lee, *Chemosphere*, 2021, **284**, 131314.
- 14 B. Farahani, M. Giahi, M. H. Ghorbani, R. Fazaeli and O. Moradi, *J. Nanostruct. Chem.*, 2023, **13**, 303–320.
- 15 M. Massaro, R. Noto and S. Riela, *Molecules*, 2020, **25**, 4863.
- 16 H. Zhang, *Nanotechnol. Rev.*, 2017, **6**, 573–581.
- 17 R. T. De Silva, R. K. Dissanayake, M. Mantilaka, W. Wijesinghe, S. S. Kaleel, T. N. Premachandra, L. Weerasinghe, G. A. J. Amaratunga and K. M. N. de Silva, *ACS Appl. Mater. Interfaces*, 2018, **10**, 33913–33922.
- 18 Y. Song, P. Yuan, P. Du, L. Deng, Y. Wei, D. Liu, X. Zhong and J. Zhou, *Appl. Clay Sci.*, 2020, **186**, 105350.
- 19 Y. Zhang, F. Zhang, Z. Yang, H. Xue and D. D. Dionysiou, *J. Catal.*, 2016, **344**, 692–700.
- 20 H. Wei, C. Hou, Y. Zhang and Z. Nan, *Sep. Purif. Technol.*, 2017, **189**, 153–161.
- 21 S. Wang, B. Yang and Y. Liu, *J. Colloid Interface Sci.*, 2017, **507**, 225–233.
- 22 K. Kuśmierek, A. Świątkowski, E. Wierzbicka and I. Legocka, *Molecules*, 2024, **29**, 3099.
- 23 W. J. Liu, Y. Zhou, W. Gong, T. T. Tang, Y. Yang, C. Yao, S. X. Zuo and X. Z. Li, *J. Appl. Chem. Biotechnol.*, 2025, **100**, 625–634.
- 24 Y. Du and P. Zheng, *Korean J. Chem. Eng.*, 2014, **31**, 2051–2056.
- 25 W. S. Wang, H. Y. Xu, B. Li, L. Y. Dai, S. Q. Zhang, Y. Xu and S. Y. Qi, *Mater. Today Commun.*, 2023, **36**, 106821.
- 26 R. Cheng, H. Li, Z. Liu and C. Du, *Minerals*, 2018, **8**, 387.
- 27 H. Zhao, H. Fu, X. Yang, S. Xiong, D. Han and X. An, *Int. J. Hydrogen Energy*, 2022, **47**, 8247–8260.
- 28 S. Mondal, S. Das and U. K. Gautam, *J. Colloid Interface Sci.*, 2021, **603**, 110–119.
- 29 S. Gedi, S. Alhammadi, J. Noh, V. R. M. Reddy, H. Park, A. M. Rabie, J. J. Shim, D. Kang and W. K. Kim, *Nanomaterials*, 2022, **12**, 282.

- 30 L. Jin, Q. Sun, Q. Xu and Y. Xu, *Bioresour. Technol.*, 2015, **197**, 348–355.
- 31 S. Lin, S. Li, Y. Zhang, T. Ma and H. Huang, *J. Mater. Chem. A*, 2021, **9**, 17936–17944.
- 32 S. De Gisi, G. Lofrano, M. Grassi and M. Notarnicola, *Sustainable Mater. Technol.*, 2016, **9**, 10–40.
- 33 X. Bian, X. Lu, Y. Xue, C. Zhang, L. Kong and C. Wang, *J. Colloid Interface Sci.*, 2013, **406**, 37–43.
- 34 F. Duan, Y. Zhu, Y. Lu, J. Xu and A. Wang, *J. Environ. Sci.*, 2023, **127**, 855–865.
- 35 S. Sadjadi, *Appl. Clay Sci.*, 2020, **189**, 105537.
- 36 D. Gu, W. Liu, J. Wang, J. Yu, J. Zhang, B. Huang, M. N. Rumyantseva and X. Li, *Chemosensors*, 2022, **10**, 165.
- 37 T. Islam, M. R. Repon, T. Islam, Z. Sarwar and M. M. Rahman, *Environ. Sci. Pollut. Res. Int.*, 2023, **30**, 9207–9242.
- 38 W. Zhang, Y. Wang, W. Tao, H. Guan, C. Jiang, W. Tian and L. Hao, *ACS Appl. Energy Mater.*, 2024, **7**, 2504–2513.
- 39 Q. Le and Z. Cheng, *Colloids Surf., A*, 2022, **655**, 130242.
- 40 M. Varga, T. Izak, V. Vretenar, H. Kozak, J. Holovsky, A. Artemenko, M. Hulman, V. Skakalova, D. S. Lee and A. Kromka, *Carbon*, 2017, **111**, 54–61.
- 41 N. V. Chukanov, S. M. Aksenov and I. V. Pekov, *Spectrochim. Acta, Part A*, 2023, **287**, 121993.
- 42 A. Saadati and S. Sheibani, *Ceram. Int.*, 2022, **48**, 30294–30306.
- 43 T. Ou, Y. Wu, W. Han, L. Kong, G. Song, D. Chen and M. Su, *J. Hazard. Mater.*, 2022, **424**, 127208.
- 44 M. Ismael, *Chem. Phys. Lett.*, 2020, **739**, 136992.
- 45 X. He, T. He, Y. Liu, Y. Zhou, B. Song, Y. Qi, L. Jiang, F. Liao and Z. Kang, *Appl. Surf. Sci.*, 2022, **606**, 154936.
- 46 Y. Liu, X. Yang, J. Ai, Q. Shang, D. Wang and G. Liao, *Chem. Eng. J.*, 2023, **474**, 145586.
- 47 F. Meng, J. Qin, H. Zhang, X. Xiong and R. Hu, *Appl. Surf. Sci.*, 2023, **623**, 157028.
- 48 M. S. Yilmaz, *Microporous Mesoporous Mater.*, 2022, **330**, 111570.
- 49 E. h. Yang and D. J. Moon, *Top. Catal.*, 2017, **60**, 697–705.
- 50 X. Zhang, R. Zhang, S. Niu, J. Zheng and C. Guo, *J. Colloid Interface Sci.*, 2019, **554**, 229–238.
- 51 L. Deng, P. Yuan, D. Liu, P. Du, J. Zhou, Y. Wei, Y. Song and Y. Liu, *Appl. Clay Sci.*, 2019, **181**, 105240.
- 52 Y. Li, B. Yu, Z. Hu and H. Wang, *Chem. Eng. J.*, 2022, **429**, 132105.
- 53 F. Chen, L. Ma, B. Li, P. Jiang, Z. Song and L. Huang, *Nanomaterials*, 2022, **12**, 2352.
- 54 M. A. Rahman, D. Lamb, M. M. Rahman, M. M. Bahar, P. Sanderson, S. Abbasi, A. Bari and R. Naidu, *J. Hazard. Mater.*, 2021, **409**, 124488.
- 55 J. Villarroel-Rocha, D. Barrera, J. J. Arroyo-Gómez and K. Sapag, *Adsorption*, 2021, **27**, 1081–1093.
- 56 R. Ezzati, *Chem. Eng. J.*, 2020, **392**, 123705.
- 57 O. V. Ovchinnikov, A. V. Evtukhova, T. S. Kondratenko, M. S. Smirnov, V. Y. Khokhlov and O. V. Erina, *Vib. Spectrosc.*, 2016, **86**, 181–189.